CrystEngComm

Accepted Manuscript

ROYAL SOCIETY OF CHEMISTRY

www.rsc.org/crystengcomm

Cite this: DOI: 10.1039/c0xx00000x

www.rsc.org/xxxxxx

ARTICLE TYPE

Self-produced bubble-template synthesis of La_2O_3:Yb/Er@Au hollow spheres with markedly enhanced luminescence and release properties

Ruichan Lv, Guixin Yang, Yunlu Dai, Shili Gai, Fei He, and Piaoping Yang*

Received (in XXX, XXX) XthXXXXXXXXX 20XX, Accepted Xth XXXXXXXXX 20XX

DOI: 10.1039/b000000x

In this report, we for the first time reported a self-produced bubble-template synthesis of La_2O_3:Yb/Er hollow mesoporous spheres (HMSs) through a facile one-step co-precipitation process. The temperature decides the bubble formation, citric acid and NaOH which determine the dispersibility are the main factors to the formation of La_2O_3:Yb/Er HMSs. Au nanocrystals (NCs) with a particle size of 9 nm were conjugated to the as-prepared HMSs without adding any organic reagents. It is noted that the up-conversion (UC) luminescence intensity of La_2O_3:Yb/Er@Au was markedly improved by 49.7-fold under low pump power. And the lifetime has been greatly enhanced due to the local field enhancement (LFE) of Au NCs, which effectively prevents the energy transfer from La_2O_3:Yb/Er to Au nanoparticles (NPs). The enhanced properties have been successfully proved by the discrete-dipole approximation (DDA) simulation. The as-prepared La_2O_3:Yb/Er@Au HMSs with large surface area (118 m^2/g) and mesoporous feature (2.92 nm in pore size) exhibit good compatibility. In addition, doxorubicin (DOX) release property and obvious cytotoxicity to MCF-7 tumor cells reveal the potential application as drug carrier. In particular, the facile and mass-production synthetic strategy may pave the way for the production of a wide class of materials.

1. Introduction

Hollow mesoporous spheres (HMSs) with functional properties have aroused intense interest because they were widely applied in various biological fields, such as drug carrier,[1–3] cell imaging,[4,5] photodynamic therapy[6,7] and gene delivery[8–10] due to their distinct low density, high specific surface area and particular porous structure.[11] Most of researches on the hollow mesoporous spheres have focused on template-directed synthesis, including both hard- and soft-template routes. Because hard-template method is complicated to proceed with low yield, and the removal of the as-used template often brings about environmental concerns and energy consumption. Therefore, scientists are tending to find simple and easy methods to produce hollow spheres using the soft template routes.[12,13]

Bubbles dispersed in a liquid host can be used to create stable emulsions and foams, which have recently emerged as promising soft templates for the synthesis of an increasing number of hollow spheres.[14] By blowing a mixed gas (O_2, CO_2 or N_2) into a solution, some of the hollow spheres were prepared by the formed bubble-template.[15,16] Another special type is the sono-chemical synthesis of hollow particles, where the gas bubbles generated from the collapse of the acoustic cavitation serve as the soft templates for shell formation.[17,18] However, these two synthesis procedures need special machines, thereby affected by many factors, such as particle surface properties, particle size, electrostatic interactions, and hydrodynamic conditions. In addition, the direct assembly and fabrication of controlled functional structures is not only of scientific interest but of down-to-earth practicality to the applied industry with such benefits as cost and energy savings.[19,20] Therefore, it is highly meaningful to find new methods to produce self-produced bubble templates without using special device.

Multi-functional rare earth oxide HMSs have been widely used as fluorescent materials for versatile bioimaging and therapy due to their unique physical and chemical characteristics resulting from the 4f electronic shells.[21–27] However, the hollow structure usually decreases the luminescent intensity as a kind of surface defect, resulting the limitation of their applications. Therefore, it aroused wide attention on the development of functional products.[28–34] Plasmonic modulation is an effective way to regulate the luminescence of these samples.[35–40] The surface plasmon resonance (SPR) of Au NCs arising from the collective oscillation of electrons on Au NCs can have beneficial or deleterious effect depending on the wavelength of the SPR peak and the distance between the UC NCs and Au NCs.

There are three considerations to ensure the enhancement effect of Au NPs. Firstly, if the SPR peak of the metal is in the near-infrared (NIR) region which is the excitation of the UC NPs, enhancement will be occurred.[41–43] Usually, the enhancement effect of nanorods is predicted to be the strongest of all the different shapes of Au NCs as they have wide and strong absorption in NIR region. While for HMSs, the nanorod may change the morphology and the structure, thus Au nanospheres who have similar morphology instead of nanorods have been

utilized.[44,45] The second one is inhibiting the deleterious SPR effect by changing the distance between the Au NCs and the UC NCs. Scientists have minimized gold-induced UC quenching or SPR transfer from UC NPs to Au NPs through preventing the direct contact between the two components by virtue of the layer of organics with a critical distance.[46-48] Thirdly, it is meaningful if the Au NCs enter the matrix, the increased disorder will incorporate variations of the direct band gap and Urbach energy, which could improve the emissions.[49] In this condition, the local field enhancement (LFE) effect could achieve unselectively enhanced multicolour UC emissions in uniform UC NCs by enhancing the excitation as the penetrating NIR wave.[50–52] In this regard, it is interesting to make the Au NCs integrate with the morphologically similar UC NCs to generate this disorder as well as LFE. Thereby, substantially increasing the excitation flux *via* LFE effect could be realized. Besides that, the DDA simulation is a flexible method for computing the absorption and scattering components of the extinction which works by simulating the NPs as a defined array of polarizable points.[53] Through simulation, the local electric field can be acquired as a result of the dipole interaction.

Herein, we first proposed a self-produced bubble template process for the synthesis of La_2O_3:Yb/Er mesoporous hollow microspheres. The influence of reaction temperature and citric acid/NaOH on bubble formation and dispersibility are discussed in detail. And the novelty of this synthetic method is characterized by a one-pot co-precipitation combining the self-assembly and the formation of mesoporous hollow structure under mild conditions, which is efficient, controllable and high-producing. Meanwhile, Au NCs with an average size of 9 nm were directly modified to La_2O_3:Yb/Er HMSs without organic additives. UC luminescent properties (the intensity, the enhanced factor versus pump power, lifetime, and the nonradiative transition) were studied to evaluate the effect of Au NCs to the HMSs. And DDA simulation was first utilized to calculate the influence of Au NCs on the UC emissions. In addition, MTT assay and DOX released properties of La_2O_3:Yb/Er@Au HMSs were investigated to evaluate the feasibility of this functional composite as the potential drug carrier.

2. Experimental Section

2.1. Materials and synthesis

All of the chemical reagents used in this experiment are of analytical grade without any further purification, including nitric acid (HNO_3), citrate acid (H_3Cit), sodium hydroxide (NaOH), ethanol, hydrochloric acid (HCl), sodium citrate, tannic acid, and $HAuCl_4$ (Beijing Chemical Corporation), La_2O_3, Yb_2O_3, Er_2O_3 (99.99%) (Sinopharm Chemical Reagent Co., Ltd.), phosphate buffered saline (PBS) and potassium hydrogen phthalate (PHP) (Tianjin Kermel Chemical Reagent Co., Ltd.).

Synthesis of La_2O_3:Yb/Er HMSs. In a typical process, 0.5 M $La(NO_3)_3$, $Yb(NO_3)_3$, and $Er(NO_3)_3$ were prepared by dissolving corresponding calculated oxides into HNO_3 with gradually heating. A total of 1 mL of 0.5 M nitrate with La/Yb/Er molar ratio of 94/5/1 and 1 mmol of citrate were dissolved to 30 mL deionized water in a beaker. After stirred for 5 min, 10 mL aqueous solution containing 4.8 g NaOH and 20 mL ethanol were added to the above reaction system and stirred for 10 min. Then the beaker was capped airtight and placed at 90 °C for 90 min in water bath. The resulting precipitates were separated by centrifugation, washed with deionized water, and dried in air at 60 °C for 12 h, then $La(OH)_3$:Yb/Er hollow spheres were acquired. The final product of La_2O_3:Yb/Er HMSs was obtained by further calcination at 550 °C for 4 h.

Preparation of La_2O_3:Yb/Er@Au HMSs. The negative changed gold NCs with a diameter of 9 nm were prepared by the citrate reduction method in the presence of tannic acid as reducing agent. Typically, 5 mL of 1 g/L $HAuCl_4$ was mixed with 30 mL deionized water containing 0.2 g sodium citrate and 0.03 g tannic acid and kept at 60 °C for 4 h. Then, the as-prepared La_2O_3:Yb/Er HMSs were dispersed in 20 mL of water, and 1 mL of the as-prepared gold suspension was swiftly added. After slowly rotated for 2 h, the La_2O_3: HMSs were collected by centrifugation.

***In vitro* viability of La_2O_3:Yb/Er@Au HMSs.** 5000-6000 L929 fibroblast cells were plated in 200 mL media per well in a 96-well plate, and 8 wells were left empty for blank control. Then the well plate was incubated for 24 h to allow the cells to attach to the wells at 37 °C with 5% CO_2. The La_2O_3:Yb/Er@Au spheres were sterilized via ultraviolet irradiation for 2 h, and diluting at concentrations of 7.8125, 15.625, 31.25, 62.5, 125, and 250 μg/mL, respectively. The solution with different concentration was added to the wells and incubated for another 24 h at 37 °C with 5% CO_2. Then 5 mg/mL 3-[4,5-dimethylthiazol-2-yl]-2,5-diphenyl tetrazolium bromide (MTT) solution was prepared by PBS. 20 μL solution was added to each well containing different amounts of La_2O_3:Yb/Er@Au. The plate was incubated at 37 °C for another 4 h subsequently. Viable cells make MTT reduce into formazan during this period, which can be dissolved by dimethyl sulfoxide (DMSO). After incubation, 100 mL of acidified isopropanol was added to each well, and placed on a shaking table for 5 min of 150 rpm in order to make the formazan and solvent mixed completely. The absorbance of the suspension was recorded using a microplate reader regulating to 570 nm as detecting wavelength.

2.2. DOX loading and release test

0.03 g of La_2O_3:Yb/Er@Au sample was added into 10 mL of phosphate buffered saline (PBS) and ultrasonic dispersed. After that, 2.5 mg DOX was added into the solution with slow stirring at room temperature for 24 h. The as-prepared mixture was centrifugally separated at 6000 rpm for 4 min, then the supernatant solution was kept for ultraviolet visible light analysis. 10 mL fresh PBS was replenished in the centrifugal tube, and set in the water bath kettle with 37 °C with magnetic stirring for 10 min, the supernatant solution was kept. The process was repeated and changed release time as 1 h, 2 h, 3 h, 4 h, 5 h, 8 h, 12 h, 24 h and 32 h, respectively. PBS (pH = 7) and potassium hydrogen phthalate (PHP) (pH = 4) was prepared directly by pH modifier. The mass of the released DOX was obtained by the absorbance with the specified 480 nm.

2.3. *In vitro* cytotoxicity of La_2O_3:Yb/Er@Au HMSs

MCF-7 cells were plated out in 96-well plates at a density of 8000 cells per well and grew overnight to make cells attached. La_2O_3:Yb/Er@Au, DOX-La_2O_3:Yb/Er@Au and DOX were

added to the medium respectively, and the cells were incubated in 5 % CO_2 at 37 °C for 24 h. The concentrations of DOX were regulated to 0.3125, 0.625, 1.25, 2.5 and 5 μg/mL. At the end of the incubation process, 20 μL of MTT solution was added into each cell and incubated for another 4 h. The supernatant in each well was aspirated and 150 μL of DMSO was added before the plate was examined using a microplate reader (Therom Multiskan MK3) at the wavelength of 490 nm.

2.4. UC luminescence microscopy (UCLM) observation

UC luminescence imaging of MCF-7 cells (5×10^4/well) were seeded in 6-well culture plates, and then incubated overnight as a monolayer. After that, these cells were incubated at 37 °C with La_2O_3:Yb,Er@Au. The cells were washed with PBS solution 3 times, fixed with 1 mL of 2.5% formaldehyde in each well for 10 min at 37°C. After that, the as-prepared cells were washed with PBS three times in order to remove attached NCs.

2.5. DDA calculations

In this work, the DDA starts by dividing the object of interest into a cubic array of N-point dipoles. Optical constants for Au and the refractive index dispersion of Au spheres with different wavelengths were used. Spherical target is subdivided with an array of cubic cells. After the interaction solved iteratively between polarizable point dipoles in the cells and the incident light with different wavelengths, the cross sections for extinction and scattering can be generated. When there are more than one Au spheres, the effective radius was calculated as $a_{eff} \equiv (3V/4\pi)^{1/3}$, where V is the volume of the target. We have looked into the Visible-Near-infrared region (400-1200 nm). The DDA is converged to a percent when the number of dipoles is larger than 10^3 with 1000 dipoles nm^{-3} in order to ensure accuracy.

2.6. Characterization

Powder X-ray diffraction (XRD) measurements were performed on a Rigaku D/max TTR-III diffractometer at a scanning rate of 15°/min in the 2θ range from 20° to 80°, with graphite monochromatized Cu Kα radiation (λ = 0.15405 nm). Images were obtained digitally on scanning electron microscope (SEM, JSM-6480A), transmission electron microscopy (TEM, FEI Tecnai G^2 S-Twin) and high-resolution transmission electron microscopy (HRTEM). N_2 adsorption/ desorption isotherms were obtained on a Micromeritics TriStar 3020 apparatus. UC emission spectra were acquired using a 980 nm LD Module (K98D08M-30W, China) as the excitation source and detected by R955 (Hamamatsu) from 400 to 800 nm. DOX concentration and the absorbance of gold NCs solution were detected by UV-1601 spectrophotometer. The measurements above were wholly performed at room temperature.

3. Results and discussion

3.1. Phase, structure and morphology

Fig. 1 shows the XRD patterns of the samples. On the basis of the Joint Committee on Power Diffraction Standard (JCPDS) reference database, the diffraction peaks of the precursor are well indexed to hexagonal $La(OH)_3$ (JCPDS No. 36–1481). And the diffraction peaks of the final product matches well with the hexagonal-phased La_2O_3 (JCPDS No. 05–0602) and cubic Au

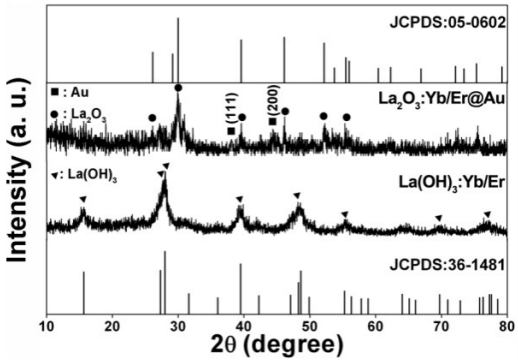

Fig. 1 XRD patterns of $La(OH)_3$:Yb/Er precursor and La_2O_3:Yb/Er@Au HMSs.

(JCPDS No. 04–0784). Meanwhile, the relatively wide peaks suggest the small nature of the samples. The average crystallite sizes are calculated from the Scherrer formula: $D_{hkl} = K\lambda/(\beta \cos\theta)$, where K is a constant (0.89), θ is the diffraction angle, β is the full-width at half-maximum, and D_{hkl} means the crystallite size along the (hkl) direction. The crystal plane (100) at $2\theta = 27.97°$ of $La(OH)_3$ and (101) at $2\theta = 29.96°$ of La_2O_3 were used to calculate the crystal size (D) of the samples. The crystallite sizes of the tiny NCs which consist of $La(OH)_3$:Yb/Er and La_2O_3:Yb/Er@Au HMSs are calculated to be 8.3 nm and 7.9 nm, respectively. The amount of Au nanocrystals attached to the La_2O_3:Yb/Er HMSs is 1.19 wt.% determined by the ICP analysis.

In the SEM image of La_2O_3:Yb/Er@Au HMSs (Fig. 2A), the sample consists of relatively uniform microspheres with an average size of 180 nm. EDS of La_2O_3:Yb/Er@Au (Fig. 2B) shows that the sample contains La, O, Yb, Er, and Au elements. In the TEM images (Fig. 2C, D), the dark shell and bright core reveal hollow structure, and the shell thickness is calculated to be about 30 nm. Close observation reveals the hollow spheres are composed of tiny particles with size of 5–10 nm, which is well consistent with the XRD results. TEM images also reveal the large number of voids in the hollow spheres. In order to confirm the successful conjunction of Au NCs on La_2O_3:Yb/Er HMSs, La_2O_3:Yb/Er@Au sample was dissolved in HCl solution for 1 min, and the TEM image of as-obtained sample is given in Fig. S1. As shown, free and attached Au NCs with size of 5–10 nm are detected. In the HRTEM image (Fig. 2E), the obvious interplanar distance of 0.24 nm between the adjacent lattice fringes agree well with the d_{111} spacing value of cubic Au (JCPDS No. 04–0784), while the distance of 0.30 nm corresponds to the d_{101} spacing value of cubic La_2O_3 (JCPDS No. 05–0602).

Fig. S2 shows SEM images of $La(OH)_3$:Yb/Er prepared at different temperatures (70 °C and 90 °C) with 2.4 g NaOH for 90 min. It is found that when the temperature is lower than the boiling point (72 °C), no hollow spheres are formed. This is because no bubbles forms when the solution is not supersaturated, and the solid spheres co-precipitated directly without the bubble template. It is known that nano-bubbles can form when a hydrophobic surface is exposed to an aqueous medium which is supersaturated with gas. Super-saturation of a gas can be achieved by displacing a liquid with another that has a lower solubility of the gas.[54] Thus we chose ethanol which possesses higher gas solubility instead of water. When the temperature is fixed at 90 °C, the mixed solution is supersaturated with a

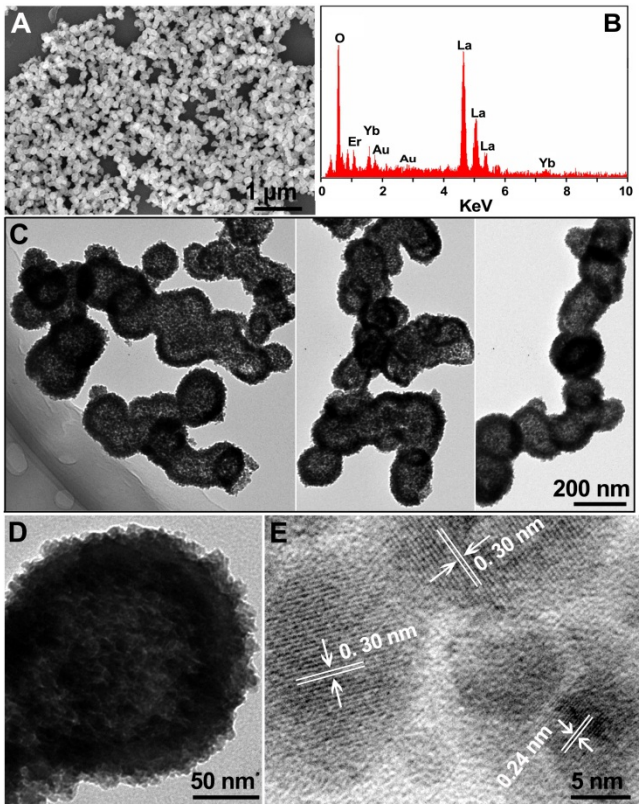

Fig. 2 SEM image (A), EDS (B), TEM images with different magnifications (C-D), and HRTEM image (E) of La_2O_3:Yb/Er@Au HMSs.

saturated vapour pressure of 157.3 KPa which is higher than the barometric pressure, then generating hollow spheres.

Citric acid has been used as a kind of surfactant to control the morphology of $La(OH)_3$:Yb/Er precursor. Fig. S3 gives the SEM images of $La(OH)_3$:Yb/Er prepared with different amount of citric acid. It is obvious that only bulk generated without H_3Cit added (Fig. S3 A1-A2). When 1 mmol H_3Cit is added, hollow spheres are produced (Fig. S3 B1-B2). Further increasing the amount of surfactant, the as-formed $La(OH)_3$:Yb/Er consists of solid spheres with apparent agglomeration (Fig. S3 C1-C2). Thus, it is essential to control the molar amount of the surfactant. On the one hand, H_3Cit plays the main role to form the complex of La^{3+} with Cit^{3-}. Without sufficient amount of stabilizing ligand, the La^{3+} and NaOH aggregate and precipitate from the solution.[55] On the other hand, the excessive amounts of H_3Cit make the micro-spheres conglutinate together, which is disadvantaged to the mono-dispersed spheres to keep stable on the bubble. In consequence, 1 mmol of H_3Cit is moderate to obtain uniform hollow spheres.

The morphologies of $La(OH)_3$:Yb/Er prepared with different amounts of NaOH at 90 °C with 1 mmol of H_3Cit are shown in Fig. 3. When 2.4 g NaOH was added, the product is composed of yolk-type HMSs. When the amount was increased to 4.8 g, hollow spheres are obtained. When further increasing the added amount to 7.2 g, there are only solid spheres. For the morphology ot the products, NaOH has two aspects of effect, the first is as reactant, and the second one is to increase the electric charge of spheres in order to stabilize the spheres through increasing the ζ

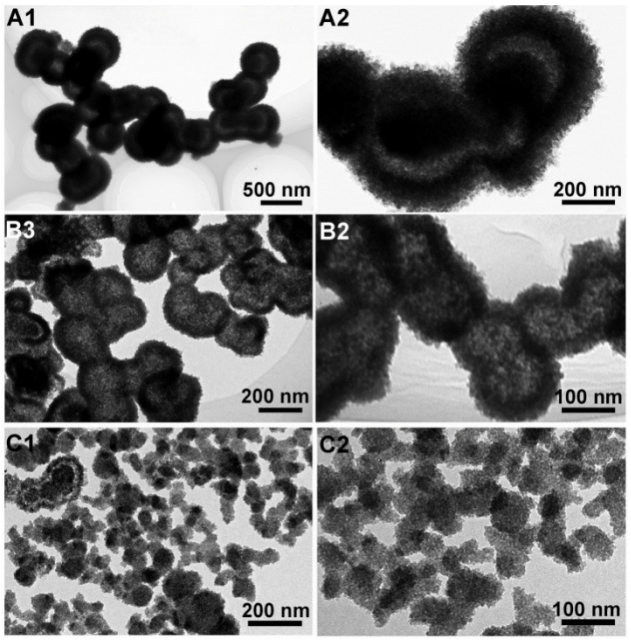

Fig. 3 TEM images of $La(OH)_3$:Yb/Er with different amounts of NaOH, 2.4 g (A1 and A2), 4.8 g (B1 and B2), and 7.2 g (C1 and C2) at 90 °C with 1 mmol of H_3Cit.

charge of the bubble and the $La(OH)_3$:Yb/Er surface.[56] The higher ζ charge results in higher electrostatic repulsion of the charged nano-spheres, and thus the as-prepared $La(OH)_3$:Yb/Er spheres are separated from each other, making the reaction system stable.[57] When the amount of NaOH is appropriate (4.8 g), the stable bubbles are generated with uniform size, then $La(OH)_3$:Yb/Er hollow spheres with ζ charge of -42.0 mV are formed. While the excess charge deriving from the superfluous NaOH will make the repulsion too be high to form La-Cit-OH^- complex on the surface of bubbles, and there are only solid spheres.

In order to ascertain the formation of a mesoporous structure, N_2 adsorption/ desorption of La_2O_3:Yb/Er@Au HMSs was measured and the isotherm is depicted in Fig. 4. It can be seen that the sample exhibits a IV-type isotherm with H1 hysteresis loops, which is the characteristic of typical mesoporous materials.[58] The specific surface area, total pore volume, and average pore width are 118 m^2/g, 0.187 cm^3/g, and 2.92 nm, respectively. The mesopore and hollow structure of the sample could provide the

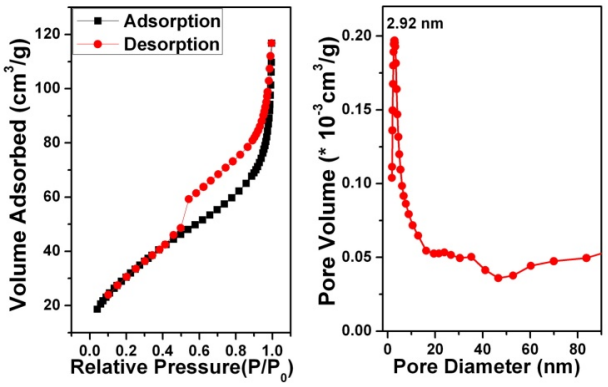

Fig. 4 Nitrogen adsorption/desorption isotherm of La_2O_3:Yb/Er@Au HMSs (A), and corresponding pore size distribution curve (B).

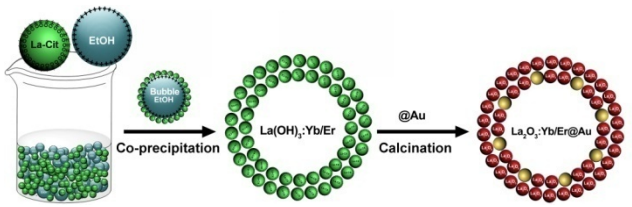

Scheme 1 The schematic diagram for the formation of La_2O_3:Yb/Er@Au HMSs.

potential capability to be employed as a drug carrier for loading and carrying drug molecules.

As discussed above, the formation of La_2O_3:Yb/Er@Au HMSs can be illustrated by three steps (Scheme 1), including the formation of negative-charged $La(OH)_3$:Yb/Er and positive-charged ethanol bubbles, the electrostatic attachment of NPs on the bubble/liquid interface, and further aggregation to form compact shells around the gas bubbles. Finally La_2O_3:Yb/Er HMSs are obtained after the annealing process, and then gold NPs with the size of 9 nm are conjugated leading to the formation of La_2O_3:Yb/Er @Au HMSs.

3.2. Photoluminescence properties

The UC emission spectra of La_2O_3:Yb/Er and La_2O_3:Yb/Er@Au under 980 nm excitation are shown in Fig. 5A. Both spectra contain three chief emission peaks at around 523, 549 and 661 nm, corresponding to respective $^2H_{11/2} \rightarrow {}^4I_{15/2}$, $^4S_{3/2} \rightarrow {}^4I_{15/2}$ and $^4F_{9/2} \rightarrow {}^4I_{15/2}$ transition of Er^{3+}.[59,60] It should be noted that the emission intensity of La_2O_3:Yb/Er@Au is markedly enhanced compared with that of La_2O_3:Yb/Er. And the enhanced intensity ratio between La_2O_3:Yb/Er@Au and La_2O_3:Yb/Er for 523, 549, and 661 nm emissions are 23.9, 19.3, and 16.8, respectively. Additionally, an emission peak at 409 nm assigned to $^2H_{9/2} \rightarrow {}^4I_{15/2}$ can be detected. In general, the emission is not observed because of the low efficiency of the three- or four-photon UC process and strong scattering of the host lattices. The obvious 409 nm emission peak suggests that the LFE of Au NCs increases the excitation process of Yb^{3+}, and thus enhancing the UC processes involving more photons.[61] There are two alternative or corporate major effects when Au NCs approach to a phosphor:

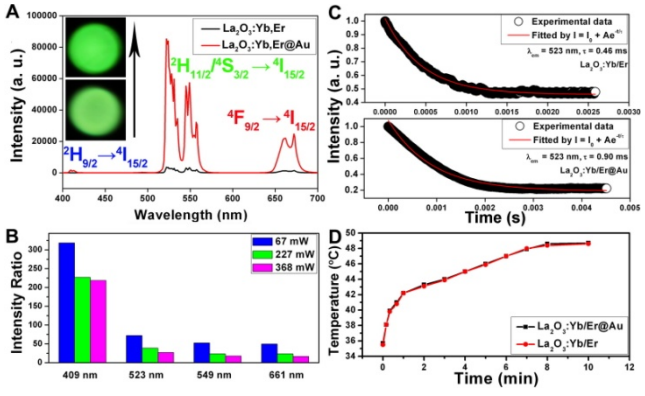

Fig. 5 UC luminescence spectra of La_2O_3:Yb/Er and La_2O_3:Yb/Er@Au HMSs (A), and the intensity ratio between the two samples under different pump power (B), the Decay curves (C) and the temperature with time increased (D) of La_2O_3:Yb/Er and La_2O_3:Yb/Er@Au HMSs under 980 nm excitation.

(1) LFE in the excitation increases the emission efficiency of UC NCs due to the increased disorder and energy deduced from Au NCs to the matrix, (2) SPR absorption in the emission reduces fluorescence of the phosphor by energy transfer from the phosphor to Au NCs. These two effects can change both the fluorescence lifetime and the intensity. And the whole enhancement in the emission spectra is attributed to LFE effect. In this case, the pump power density of 980 nm excitation can be increased by LFE enhancement of Au NCs, resulting in the increase of excited Yb^{3+} ions. When no Au NCs is modified, the excitation of Yb^{3+} ions is much lower, and the blue energy transfer is not able to appear as it need three- or four-photon transfer. The UV-vis absorbance of Au NCs is shown in Fig. S4A, and we can see there is a wide peak around 530 nm. No decreased intensity ratio (Fig. S4B) occurs in the local absorbance of gold due to the SPR effect, which transfers some transitions of Er^{3+} to Au NCs.

Fig. 5B gives the enhanced UC emission intensity ratio excited with different pump power, and the corresponding emission spectra are presented in Fig. S5. We can see that under low pump power of 67 mW, the intensity ratio for 409, 523, 549, and 661 nm emissions are 318.6, 72.1, 52.5, and 49.7, respectively. It is well accepted that the output luminescent intensity (I) is a function of the NIR excitation power (P), which is signified by the formula of $I \propto P^n$, where n is the absorbed photon numbers by the ground-state level during the energy-transfer process. Assuming that the local field enhancement factor (LFEF) is 4.5, for the three- or four-photon blue emission at 409 nm, according to $I \propto (4.5P)^{3-4}$, the intensity ratio is 91-fold, and for the two-photon emission at 523 nm, the ratios is about 20-fold, which is well consistent with the measured result as shown in Fig. 5B. Meanwhile, the ratios under 67 mW are higher than that of the value under the stronger pump power of 406 mW in Fig. 5A. This reveals that the enhancement of UC emissions has been enhanced more under lower pump power, which can be attributed to the higher LFEF under the lower pump power.[61]

Fig. 5C presents the decay curves of Er^{3+} ions in La_2O_3:Yb/Er and La_2O_3:Yb/Er@Au at 523 nm under 980 nm excitation. Both decay curves can be well fitted into the single exponential function of $I = I_0 + A \exp(-t/\tau)$ (where τ is the 1/e life time of the Er^{3+} ion). The result indicates that the lifetime of Er^{3+} ions increased from 0.46 to 0.90 ms after attaching Au NCs to the surface of La_2O_3:Yb/Er. This enhancement of emission efficiency can be attribute to the coupling of the UC process, which effectively increases both the non-radiative and radiative decay rates arising from SPR.[47] The prolonged lifetime is evidently not in agreement with the character of simple SPR effect of Au NCs in which the transition of Er^{3+} ions decays fast.[62] Fig. 5D presents temperatures of La_2O_3:Yb/Er and La_2O_3:Yb/Er@Au with the increased time. The two samples show similar temperatures under NIR irradiation, indicating no nonradiative transition occurs for La_2O_3:Yb/Er@Au due to the SPR effect, and the same increased temperature can be ascribed to the nonradiative of Er^{3+} ions. The results confirm that there is no SPR from La_2O_3:Yb/Er to Au NCs, which will be proved by the following DDA simulation.

DDA calculation was used to investigate and predict the SPR peak and the strength of LFE. The absorbance spectrum of the Au NCs with the diameter of 10 nm for the experiment is shown in

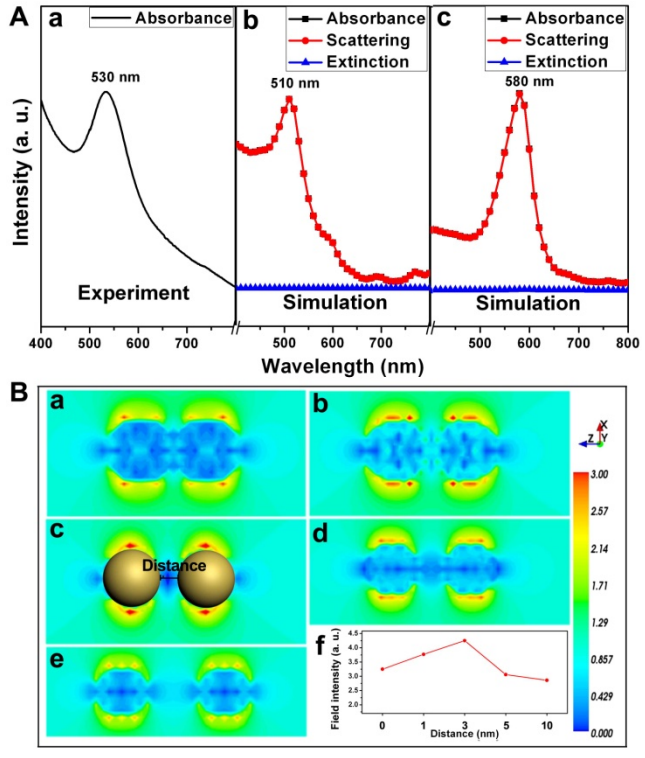

Fig. 6. The intensity of single Au nanosphere with different wavelengths of the experiment and the simulation (A). The electric field strength ($|E|/|E_0|$) of two ANs at the wavelength of 980 nm with the different distances between the two spheres (B).

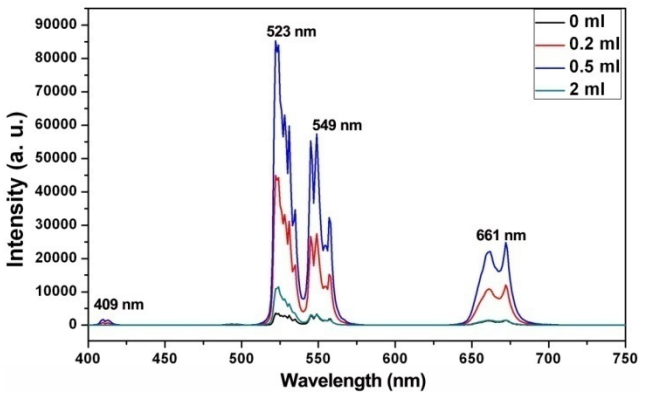

Fig. 7 The intensities of La_2O_3:Yb/Er@Au HMSs with different amount of Au solution.

Fig. 6Aa and the simulation result is given in Fig. 6Ab. It is found that both spectra are much similar. For the experiment, the region of the absorption peak is slight larger than that of the simulated value due to the single direction in simulation condition.

Besides, the scattering spectrum of Au NCs is negligible, which indicates the absorbance plays a main role when the Au NCs has small diameter. The as-prepared La_2O_3:Yb/Er@Au comprising of Au and La_2O_3:Yb/Er increases the refractive index of the surroundings (assumed to 1.8), because the air medium is replaced by La_2O_3:Yb/Er. Fig. 6Ac shows the intensities with the refractive index of 1.8, and the SPR peak translates to 580 nm. This translation prevents SPR transfer from La_2O_3:Yb/Er to Au NCs, thus no decrease occurs in the transitions of $^2H_{11/2} \rightarrow {}^4I_{15/2}$

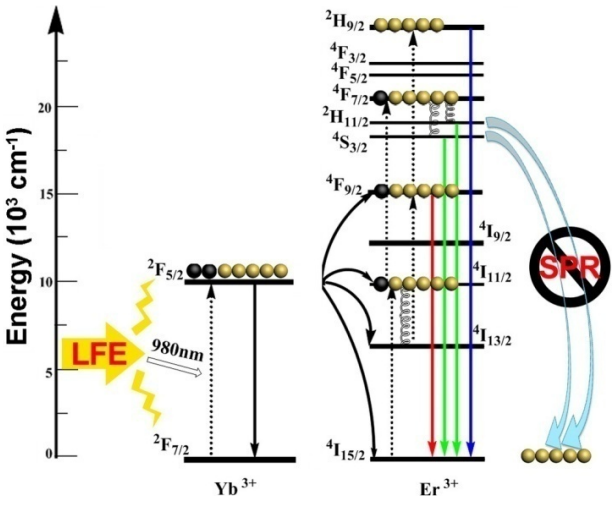

Fig. 8 The energy-transfer mechanism of La_2O_3:Yb/Er@Au using the energy level diagram.

(523 nm) and $^4S_{3/2} \rightarrow {}^4I_{15/2}$ (549 nm). Fig. 6B presents the electric field strength ($|E|/|E_0|$) at λ = 980 nm with different distances between two spheres. We can see that the strength has a maximum value at the distance of 3 nm. The experimental data is given in Fig. 7. When the amount of Au solution is increased to 0.5 mL, the distance between the Au NCs reduce to a critical value, and the intensity of La_2O_3:Yb/Er@Au has the highest value. That means the LFE has the maximum value when was detected at a critical distance. The result of DDA simulation coincides well with the experiment results.

The energy-transfer mechanism of La_2O_3:Yb/Er@Au is given in Fig. 8 using the energy level diagram. The remarkably enhanced UC emissions and prolonged lifetimes without any nonradiative transition are mainly achieved by the effect of LFE enhancement from the disorder of Au NCs to La_2O_3:Yb/Er, resulting in the increase of excited Yb^{3+} ions. The SPR effect is prevented due to the critical distance separated by pores. Excited photons increased more under the lower pump powers with the Au nanocrystals added. When the pump power increased, the photons in the excited levels may saturate, and the enhancement factor decreases. In this case, the UC emission intensity of La_2O_3:Yb/Er@Au can be greatly high under lower pump power. As we know that the desired UC materials for biological applications should be of low pump threshold in power density and show high efficiency for UC emissions.[51] In this regard, the as-prepared La_2O_3:Yb/Er@Au HMSs should be excellent biological materials.

3.3. Cell viability and Drug release properties

For potential biological application, it is essential to evaluate the biocompatibility of La_2O_3:Yb/Er@Au HMSs. Firstly, for the aim of application in drug delivery and bio-imaging, we have taken the photograph of the La_2O_3:Yb/Er@Au sample dispersed in the deionized water under the daylight (Fig. S6). After ultrasonic treatment and standing for 10 min, the sample kept stable which indicate the as-prepared sample is proper for the bio-application. Meanwhile, standard MTT cell assay was carried on L929 cell lines in order to detect the viability. Fig. 9 demonstrates the viability of L929 fibroblast cell incubated for 24 h with different

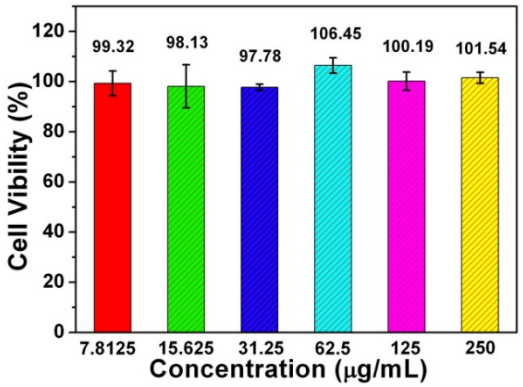

Fig. 9 The viability of L929 fibroblast cell incubated with different concentrations of La_2O_3:Yb/Er@Au HMSs.

concentrations of the particles varying from 7.8125 to 250 μg/mL. It is obviously shown that the cell viability of the as-prepared material in all dosages is up to 97.78−106.45%. Even at a high-dose concentration of 250 μg/mL, there are still 101.54% cells observed. The MTT assay demonstrated that these hollow spheres are nontoxic to live cells and can be potentially applied as drug carrier.

DOX was selected as a model drug to evaluate the loading and controlled release behaviors of hollow spheres.[63] After being continuously stirred for 24 h, DOX has been almost completely convergent to La_2O_3:Yb/Er@Au HMSs with a loading efficiency of 82.3%. Additionally, we detected the pH-dependent drug-release behavior. The pH values of 4 and 7, which represent the environments of cancer and normal cells respectively, were selected to study the drug release properties. As shown in Fig. 10, in the initial 1 h, the release efficiencies are 68.0% and 28.0%, respectively. After released for 32 h, the release efficiencies are increased to 90.5% (pH = 4) and 41.4% (pH = 7), respectively. There are two steps in the release process: the initially rapid release caused by the diffusion and the slow release due to the strong interaction between the channels of mesoporous pores and drug molecules. The initially rapid release of DOX molecules is essential to the treatment of cancer because the fast release of an anticancer drug can efficiently inhibit the growth of cancer cells. After that, the slow release of the rest of the drug molecules can kill the surviving cells from the first stage.

Fig. 11 shows that when La_2O_3:Yb/Er@Au HMSs were used as drug carrier, more than 92.4% MCF-7 cells are viable under a

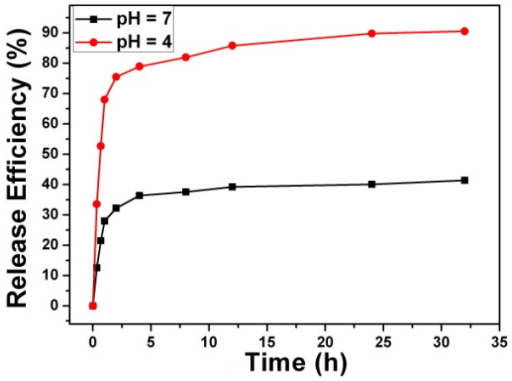

Fig. 10 The DOX release efficiency of La_2O_3:Yb/Er@Au HMSs.

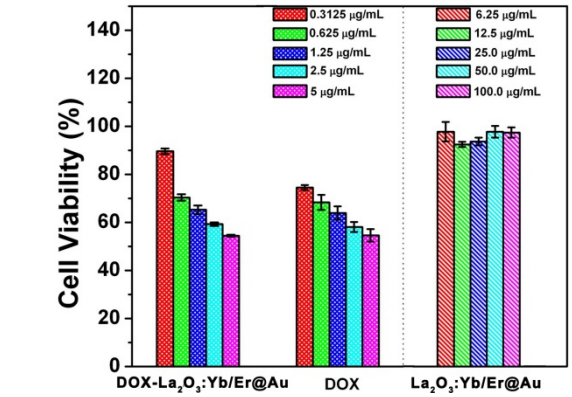

Fig. 11 The cytotoxicity incubated with MCF-7 cells.

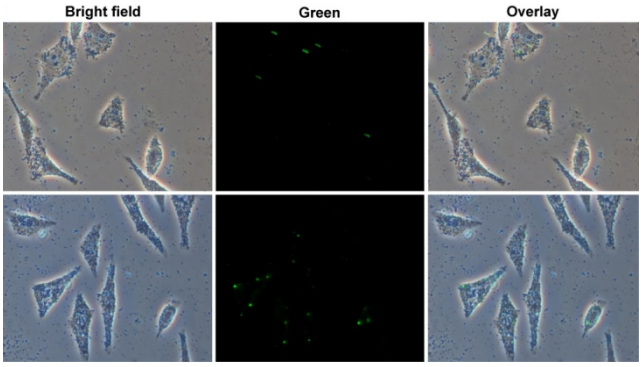

Fig. 12 The inverted fluorescence microscope images of MCF-7 cells incubated for 3h (up) and 6 h (down) of La_2O_3:Yb/Er@Au HMSs.

wide concentration range (6.25-100 μg/mL), indicating La_2O_3:Yb/Er@Au HMSs have no obvious cytotoxicity. In comparison, even with the low concentration, La_2O_3:Yb/Er@Au-DOX has high cytotoxicity to MCF-7 tumor cells, suggesting the potential as the anti-cancer drug carrier. Fig. 12 gives the inverted fluorescence microscope images of MCF-7 cells incubated with La_2O_3:Yb/Er@Au HMSs for 3 h and 6 h at 37 °C using a confocal microscope equipped with a 980 nm NIR laser. We can see all the luminescence signal of La_2O_3:Yb/Er@Au is coming from inside of the cells, and no signal outside of the cells was observed, which reveals the material has entered and been up-taken by the cells instead of just staining the membrane surface.[64–68] This further indicates the as-prepared hollow structure is favorable to drug loading as carrier.

4. Conclusions

In summary, we have successfully proposed a self-produced bubble template route for the synthesis of La_2O_3:Yb/Er@Au HMSs with highly enhanced UC emission. The size, structure and dispersibility of the as-prepared products can simply be tuned by reaction temperature, the amount of citric acid and NaOH. The luminescent intensity of La_2O_3:Yb/Er@Au HMSs has been markedly increased especially under lower pump power (at least 49.7-fold), and the lifetime was enhanced without nonradiative transition. The enhanced UC emissions are contributed to the LFE effect of Au NCs, which effectively prevents SPR from UC NPs to Au NPs due to the critical distance separated by the pores. And the enhanced properties have also been proved by the DDA simulation. MTT assay and DOX release properties of

La_2O_3:Yb/Er@Au HMSs revealed that the as-prepared sample is potentially applied as drug carrier. In particular, this self-produced bubble template method may be applied for the synthesis of other materials.

Acknowledgements

Financial supports from the National Natural Science Foundation of China (NSFC 21271053), Research Fund for the Doctoral Program of Higher Education of China (20112304110021), Natural Science Foundation of Heilongjiang Province (LC2012C10), Harbin Sci.-Tech. Innovation Foundation (RC2012XK017012), and the Fundamental Research Funds for the Central Universities of China are greatly acknowledged.

Notes and references

Key Laboratory of Superlight Materials and Surface Technology, Ministry of Education, College of Material Science and Chemical Engineering, Harbin Engineering University, Harbin 150001, P. R. China. E-mail: yangpiaoping@hrbeu.edu.cn

† Electronic Supplementary Information (ESI) available: SEM image of La_2O_3:Yb/Er@Au HMSs dissolved by HCl, SEM images of $La(OH)_3$:Yb/Er prepared at different temperatures, SEM images of $La(OH)_3$:Yb/Er prepared with different amount of H_3Cit, UV-vis spectra of ANs and the intensity ratio between the AHMSs and LHMSs, The UC emission spectra of LHMSs and AHMSs under different pump power. See DOI: 10.1039/b000000x

1 P. Yang, S. Gai and J. Lin, *Chem. Soc. Rev.*, 2012, **41**, 3679–3698.
2 Q. Lin, Q. Huang, C. Li, C. Bao, Z. Liu, F. Li and L. Zhu, *J. Am. Chem. Soc.*, 2010, **132**, 10645–10647.
3 Y. Chen, H. Chen, D. Zeng, Y. Tian, F. Chen, J. Feng and J. Shi, *Acs Nano*, 2010, **4**, 6001–6013.
4 S. Gai, C. Li, P. Yang and J. Lin, *Chem. Rev.* , 2013, 114, 2343–2389.
5 G. Jia, M. Yang, Y. H. Song, H. P. You and H. J. Zhang, *Cryst. Growth Des.*, 2009, **9**, 301–307.
6 D. Brevet, M. Gary-Bobo, L. Raehm, S. Richeter, O. Hocine, K. Amro, B. Loock, P. Couleaud, C. Frochot, A. Morere, P. Maillard, M. Garcia and J.-O. Durand, *Chem. Commun.*, 2009, 1475–1477.
7 H. L. Tu, Y. S. Lin, H. Y. Lin, Y. Hung, L. W. Lo, Y. F. Chen and C. Y. Mou, *Adv Mater*, 2009, **21**, 172–177.
8 Slowing, II, B. G. Trewyn, S. Giri and V. S. Y. Lin, *Adv. Funct. Mater.*, 2007, **17**, 1225–1236.
9 F. Torney, B. G. Trewyn, V. S. Y. Lin and K. Wang, *Nat. Nanotechnol.*, 2007, **2**, 295–300.
10 Z. Chen, H. Chen, H. Hu, M. Yu, F. Li, Q. Zhang, Z. Zhou, T. Yi and C. Huang, *J. Am. Chem. Soc.*, 2008, **130**, 3023–3029.
11 L. D. Carlos, R. A. S. Ferreira, V. d. Z. Bermudez, B. Julian-Lopez and P. Escribano, *Chem. Soc. Rev.*, 2011, **40**, 536–549.
12 C. Chen, C. Nan, D. Wang, Q. Su, H. Duan, X. Liu, L. Zhang, D. Chu, W. Song, Q. Peng and Y. Li, *Angew. Chem. Int. Ed.*, 2011, **50**, 3725–3729.
13 L. Tian, X. Yang, P. Lu, I. D. Williams, C. Wang, S. Ou, C. Liang and M. Wu, *Inorg. Chem.*, 2008, **47**, 5522–5524.
14 X. W. Lou, L. A. Archer and Z. Yang, *Adv. Mater.*, 2008, **20**, 3987–4019.
15 G. Hadiko, Y. S. Han, M. Fuji and M. Takahashi, *Mater. Lett.*, 2005, **59**, 2519–2522.
16 P. Y. Keng, B. Y. Kim, I.-B. Shim, R. Sahoo, P. E. Veneman, N. R. Armstrong, H. Yoo, J. E. Pemberton, M. M. Bull, J. J. Griebel, E. L. Ratcliff, K. G. Nebesny and J. Pyun, *ACS Nano*, 2009, **3**, 3143–3157.
17 Y. Cai, H. Pan, X. Xu, Q. Hu, L. Li and R. Tang, *Chem. Mater.*, 2007, **19**, 3081–3083.
18 W. H. Suh, A. R. Jang, Y.-H. Suh and K. S. Suslick, *Adv. Mater.*, 2006, **18**, 1832–1837.
19 N. Wang, X. Cao, D. Kong, W. Chen, L. Guo and C. Chen, *J. Phys. Chem. C*, 2008, **112**, 6613–6619.
20 X. Yu, D. Wang, Q. Peng and Y. Li, *Chem. Commun.*, 2011, **47**, 8094–8096.
21 L. Gonzalez-Rovira, J. M. Sanchez-Amaya, M. Lopez-Haro, A. B. Hungria, Z. Boukha, S. Bernal and F. J. Botana, *Nanotechnology*, 2008, **19**, 495305.
22 F. Lei, B. Yan, H. H. Chen and J. T. Zhao, *Inorg. Chem*. 2009, **48**, 7576.
23 G. Jia, Y. Zheng, K. Liu, Y. Song, H. You and H. Zhang, *J. Phys. Chem. C*, 2009, **113**, 153–158.
24 A. G. Macedo, R. A. S. Ferreira, D. Ananias, M. S. Reis, V. S. Amaral, L. D. Carlos and J. Rocha, *Adv. Funct. Mater.*, 2010, **20**, 624–634.
25 J.-C. Boyer and F. C. J. M. van Veggel, *Nanoscale*, 2010, **2**, 1417–1419.
26 X. Yang, Q. Li, Z. Liu, X. Bai, H. Song, M. Yao, B. Liu, R. Liu, C. Gong, S. Lu, Z. Yao, D. Li, J. Liu, Z. Chen, B. Zou, T. Cui and B. Liu, *J. Phys. Chem. C*, 2013, **117**, 8503–8508.
27 Y. Liu, S. Zhou, D. Tu, Z. Chen, M. Huang, H. Zhu, E. Ma and X. Chen, *J. Am. Chem. Soc.*, 2012, **134**, 15083–15090.
28 L. D. Carlos, R. A. S. Ferreira, V. d. Z. Bermudez and S. J. L. Ribeiro, *Adv. Mater.*, 2009, **21**, 509–534.
29 S. Zhang, W. Ni, X. Kou, M. H. Yeung, L. Sun, J. Wang and C. Yan, *Adv. Funct. Mater.* , 2007, **17**, 3258–3266.
30 Q. Zhao, F. Li and C. Huang, *Chem. Soc. Rev.* , 2010, 39, 3007–3030.
31 F. Wang, R. Deng, J. Wang, Q. Wang, Y. Han, H. Zhu, X. Chen and X. Liu, *Nat. Mater.*, 2011, **10**, 968–973.
32 S. Zeng, M.–K. Tsang, C.-F. Chan, K.-L. Wong, B. Fei and J. Hao, *Nanoscale*, 2012, **4**, 5118–5124.
33 Y. Liu, D. Tu, H. Zhu and X. Chen, *Chem. Soc. Rev.*, 2013, **42**, 6924–6958.
34 A. K. Sharma, K. H. Son, B. Y. Han and K.-S. Sohn, *Adv. Funct. Mater.*, 2010, **20**, 1750–1755.
35 W. Yin, L. Zhao, L. Zhou, Z. Gu, X. Liu, G. Tian, S. Jin, L. Yan, W. Ren, G. Xing and Y. Zhao, *Chem. Eur. J.*, 2012, **18**, 9239–9245.
36 G. Li, D. Geng, M. Shang, C. Peng, Z. Cheng and J. Lin, *J. Mater. Chem.*, 2011, **21**, 13334–13344.
37 Y. Zhou, B. Yan and X.-H. He, *J. Mater. Chem. C*, 2014, **2**, 848–855.
38 M. Chen, Z. Lei, W. Feng, C. Li, Q.-M. Wang and F. Li, *Biomaterials*, 2013, **34**, 4284–4295.
39 Y. Zhang and J. Hao, *J. Mater. Chem. C*, 2013, 1, 5607–5618.
40 J. Zhu, Y. Lu, Y. Li, J. Jiang, L. Cheng, Z. Liu, L. Guo, Y. Pan and H. Gu, *Nanoscale*, 2014, **6**, 199–202.
41 A. Priyam, N. M. Idris and Y. Zhang, *J. Mater. Chem.*, 2012, **22**, 960–965.
42 R. J. Amjad, M. R. Sahar, S. K. Ghoshal, M. R. Dousti, S. Riaz and B. A. Tahir, *J. Lumin.*, 2012, **132**, 2714–2718.
43 S. T. Sivapalan, J. H. Vella, T. K. Yang, M. J. Dalton, R. N. Swiger, J. E. Haley, T. M. Cooper, A. M. Urbas, L.-S. Tan and C. J. Murphy, *Langmuir*, 2012, **28**, 9147–9154.
44 D. Wawrzynczyk, A. Bednarkiewicz, M. Nyk, M. Gordel, W. Strek and M. Samoc, *Opt. Mater.*, 2012, **34**, 1708–1712.
45 P. Kannan, F. A. Rahim, R. Chen, X. Teng, L. Huang, H. Sun and D.-H. Kim, *ACS Appl. Mat. Interfaces* 2013, **5**, 3508–3513.
46 L. Cheng, K. Yang, Y. Li, J. Chen, C. Wang, M. Shao, S.-T. Lee and Z. Liu, *Angew. Chem. In. Ed.*, 2011, **50**, 7385–7390.
47 H. Zhang, Y. Li, I. A. Ivanov, Y. Qu, Y. Huang and X. Duan, *Angew. Chem. In. Ed.*, 2010, **49**, 2865–2868.
48 F. Zhang, G. B. Braun, Y. Shi, Y. Zhang, X. Sun, N. O. Reich, D. Zhao and G. Stucky, *J. Am. Chem. Soc.*, 2010, **132**, 2850–2851.
49 A. Awang, S. K. Ghoshal, M. R. Sahar, M. R. Dousti, R. J. Amjad and F. Nawaz, *Curr. Appl Phys.*, 2013, **13**, 1813–1818.
50 N. Liu, W. Qin, G. Qin, T. Jiang and D. Zhao, *Chem. Commun.*, 2011, **47**, 7671–7673.
51 Y. Zhong, C. Wang, L. Cheng, F. Meng, Z. Zhong and Z. Liu, *Biomacromolecules*, 2013, **14**, 2411–2419.
52 A. Awang, S. K. Ghoshal, M. R. Sahar, M. Reza Dousti, R. J. Amjad and F. Nawaz, *Curr. Appl Phys.*, 2013, **13**, 1813–1818.
53 M. A. Mahmoud, D. O'Neil and M. A. El-Sayed, *Chem. Mater.*, 2014, **26**, 44–58.
54 X. H. Zhang, X. Zhang, J. Sun, Z. Zhang, G. Li, H. Fang, X. Xiao, X.

Zeng and J. Hu, *Langmuir*, 2007, **23**, 1778–1783.
55 C. Dong and F. C. J. M. van Veggel, *ACS Nano*, 2009, **3**, 123–130.
56 G. Ivan Guerrero–Garcia, P. Gonzalez-Mozuelos and M. Olvera de la Cruz, *ACS Nano*, 2013, **7**, 9714–9723.
57 N. Li, Q. Zhang, J. Liu, J. Joo, A. Lee, Y. Gan and Y. Yin, *Chem. Commun.* , 2013, **49**, 5135–5137.
58 G. Jia, H. You, K. Liu, Y. Zheng, N. Guo and H. Zhang, *Langmuir*, 2010, **26**, 5122–5128.
59 J. Zhuang, L. Liang, H. H. Y. Sung, X. Yang, M. Wu, I. D. Williams, S. Feng and Q. Su, *Inorg. Chem.*, 2007, **46**, 5404–5410.
60 Z. L. Wang, J. H. Hao, H. L. W. chan and W. T. Wong, *Small*, 2012, **8**, 1863–1868.
61 H. Zhang, D. Xu, Y. Huang and X. Duan, *Chem. Commun.* , 2011, **47**, 979–981.
62 J. Bao, W. Chen, T. Liu, Y. Zhu, P. Jin, L. Wang, J. Liu, Y. Wei and Y. Li, *ACS Nano*, 2007, **1**, 293–298.
63 S. P. Sherlock, S. M. Tabakman, L. Xie and H. Dai, *Acs Nano*, 2011, 5, 1505–1512.
64 W. Zheng, S. Zhou, Z. Chen, P. Hu, Y. Liu, D. Tu, H. Zhu, R. Li, M. Huang and X. Chen, *Angew. Chem. Int. Ed.*, 2013, **52**, 6671–6676.
65 Y. Li, Y. Wu, J. Chang, M. Chen, R. Liu and F. Li, *Chem. Commun.*, 2013, **49**, 11335–11337.
66 B. Simard, B. Tomanek, F. C. J. M. van Veggel and A. Abulrob, *Photochem. Photobiol. Sci.*, 2013, **12**, 1824–1829.
67 H. Gong, L. Cheng, J. Xiang, H. Xu, L. Feng, X. Shi and Z. Liu, *Adv. Funct. Mater.*, 2013, **23**, 6059–6067.
68 Z.-L. Wang, J. Hao, H. L. W. Chan, G.-L. Law, W.-T. Wong, K.-L. Wong, M. B. Murphy, T. Su, Z. H. Zhang and S. Q. Zeng, *Nanoscale*, 2011, **3**, 2175–2181.